Nanosensors Based on a Single ZnO:Eu Nanowire for Hydrogen Gas Sensing

Cristian Lupan,* Abhishek Kumar Mishra,* Niklas Wolff, Jonas Drewes, Helge Krüger, Alexander Vahl,* Oleg Lupan,* Thierry Pauporté, Bruno Viana, Lorenz Kienle, Rainer Adelung, Nora H de Leeuw, and Sandra Hansen*

Cite This: ACS Appl. Mater. Interfaces 2022, 14, 41196–41207

Read Online

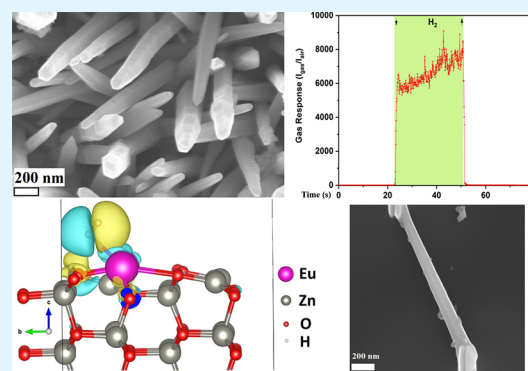ACCESS | Metrics & More | Article Recommendations | Supporting Information

ABSTRACT: Fast detection of hydrogen gas leakage or its release in different environments, especially in large electric vehicle batteries, is a major challenge for sensing applications. In this study, the morphological, structural, chemical, optical, and electronic characterizations of ZnO:Eu nanowire arrays are reported and discussed in detail. In particular, the influence of different Eu concentrations during electrochemical deposition was investigated together with the sensing properties and mechanism. Surprisingly, by using only 10 μM Eu ions during deposition, the value of the gas response increased by a factor of nearly 130 compared to an undoped ZnO nanowire and we found an H_2 gas response of ~7860 for a single ZnO:Eu nanowire device. Further, the synthesized nanowire sensors were tested with ultraviolet (UV) light and a range of test gases, showing a UV responsiveness of ~12.8 and a good selectivity to 100 ppm H_2 gas. A dual-mode nanosensor is shown to detect UV/H_2 gas simultaneously for selective detection of H_2 during UV irradiation and its effect on the sensing mechanism. The nanowire sensing approach here demonstrates the feasibility of using such small devices to detect hydrogen leaks in harsh, small-scale environments, for example, stacked battery packs in mobile applications. In addition, the results obtained are supported through density functional theory-based simulations, which highlight the importance of rare earth nanoparticles on the oxide surface for improved sensitivity and selectivity of gas sensors, even at room temperature, thereby allowing, for instance, lower power consumption and denser deployment.

KEYWORDS: Eu_2O_3, ZnO, sensor, hydrogen, electrochemical deposition
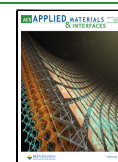
1. INTRODUCTION

Hydrogen (H_2) is an extremely useful gas that has great potential for future applications as it represents an alternative, clean, sustainable, and promising energy source for the stationary and transportation sectors.[1,2] However, hydrogen gas is also a common decomposition product of chemical reactions such as those that occur during battery operation and therefore must be detected, owing primarily to its reactivity and hazardousness.[3−5] In batteries, especially in large vehicle applications, several types of defects can increase the temperature and lead to undesirable chemical reactions that can also cause thermal runaway.[6−8] Any fault condition must be investigated and preferably prevented during operation to increase safety, as health hazards such as toxic (e.g., CO, HF) and flammable (e.g., H_2, CH_4, C_2H_4, electrolytes) gases, as well as fire and explosions, may occur.[6,7] Therefore, several research groups are investigating the gas evolution, especially of H_2 and CO, in different types of battery cells during overcharging and at high temperatures to enable the development of appropriate early warning systems. Such systems are based on new materials and are in particular relevant for detection of H_2

levels during over-temperature triggering to avoid various hazards.[4,9,10] Another major safety issue with H_2 is its ability to diffuse very easily and mix quickly with the air by diffusion. The International Fire Code (IFC) allows H_2 levels as high as 1% vol,[11] while mixing ratios of hydrogen with oxygen ranging above 4% (lower explosive limit (LEL) or the lower flammability limit (LFL)) and below 75% (upper explosive limit (UEL) or the upper flammability limit (UFL)) by volume are highly explosive and therefore dangerous.[12] Since both the hydrogen−oxygen mixture flame and combustion flames emit UV radiation, which is invisible to the human eye, a device containing a H_2 gas sensor and a UV detector as a dual-mode sensor or two separate devices are required for safety

monitoring and raising the alarm.[13] With the increasing use of hydrogen and the demand for small, cheap, and new electronic devices that can detect hazardous gases, semiconductor oxide-based multifunctional devices are one of the most relevant types for future sensing applications owing to their small size, improved safety, usually good and direct sensing response, and increased efficiency.[14] Micro- and nanodevices based on new functional oxides are now the focus of applied research, as they are expected to become the largest and fastest market, with sales exceeding trillions of euros.[13]

Zinc oxide (ZnO) is a semiconductor oxide material that is often used in sensing applications, but it suffers from poor selectivity, high operating temperature, and inadequate response. However, mixing or doping with impurities[14,15] and surface functionalization with rare earth elements, such as Ce, Eu, and Er[16−18] improves the sensing properties due to catalytic efficiency and access to oxygen ions and the high basicity of the ZnO surface.[15,19] However, technologies are needed to synthesize such a combination of oxides with rare earth elements that can be used on a larger scale. In addition, Eu^{3+} ions improve the photocatalytic properties of ZnO by reducing the recombination of electron−hole pairs[20] after creating an energy level of impurities[21] that improves the absorption properties of the material.[21] By doping ZnO with rare earth elements[15,21] and mixing and/or surface functionalization with noble metal nanoparticles, a better response and lower operating temperature have already been observed for gas sensing applications.[16−18]

ZnO doped or mixed with rare earth elements (Tb, Eu, Ce, Er, La, etc.) for sensing applications have been studied by several groups to increase the response value, control selectivity, and reduce the operating temperature.[15,22,23] Zhao et al.[22] reported the effects of doping rare earth elements in ZnO nanowires (NWs) on the sensing performances and found that ZnO NWs doped with 1% Ce responded best to ethanol. Hastir et al.[15] investigated the gas sensor properties by doping ZnO with Tb, Dy, and Er, observing significant improvement in the sensitivity to ethanol and a decrease in the operating temperature. Also, by doping ZnO with Tb and Er, a selectivity to ethanol and acetone was observed.[15] Here, the improvement in the gas sensor response was attributed to changes caused by rare earth doping, such as high surface basicity, increased surface area, morphological changes, and the presence of oxygen vacancies.[15] A reduction in the optimum operating temperature due to doping was explained by catalytic effects, which increase the reaction rate and provide various reaction pathways that possess lower activation energies toward the applied gas.[15,23] Rare earth elements, such as europium and its oxides, can enhance the sensing properties of zinc oxide due to catalytic efficiency, high mobility of oxygen ions, and basicity of the surface. However, to our knowledge, there are no reports so far of H_2 detectors or UV/H_2 dual-mode nanosensors made from such a combination of oxides.

Nanosensors, microsensors based on Eu-doped/functionalized zinc oxide, are considered to have advantages such as lower operating temperature (down to room temperature) to eliminate potential drawbacks due to heat exposure, lower device cost, and lower power consumption. In addition, nanosensors offer the important advantage of their small size, which allows them to be integrated into various devices to monitor and detect hazardous gases in multiple places on larger batteries, such as in vehicles, which is clearly a motivation for further research.

In this work, ZnO:Eu nanowire arrays were fabricated by an electrochemical deposition method and integrated into nanosensors as individual nanowires. Next, the morphological, chemical, structural, optical, and sensor properties of different concentrations of Eu in ZnO:Eu composites were investigated. The potential nanosensors for the detection of UV light and hydrogen gas detection were also evaluated for ZnO:Eu nanowire-based devices and dual-mode sensors. Density functional theory (DFT)-based simulations provided insights into Eu doping-mediated H_2 gas sensing on ZnO nanowires.

2. EXPERIMENTAL AND COMPUTATIONAL DETAILS

ZnO:Eu nanowire-networks were grown onto fluorine-doped tin oxide (FTO) films on glass substrates using an electrochemical deposition method[21,24] by mixing 0.02 M $ZnCl_2$ and 1 M KCl as precursors and different concentrations of $EuCl_3$ (3, 5, 6, 7, 8, 9, 10, and 20 μM) for mixing or surface deposition with Eu^{3+} ions in deionized water with a resistivity of 18.2 MΩ·cm. Samples were noted as Eu3 for 3 μM, Eu6 for 6 μM, and Eu10 for 10 μM $EuCl_3$ in the electrolyte, respectively.

Different sets of ZnO:Eu nanowire-networks were investigated by X-ray photoelectron spectroscopy (XPS, Omicron Nano-Technology GmbH, Al-anode, 240 W) to determine the chemical/electronic properties. The measured spectra were referenced toward the C 1s line of aliphatic carbon at 285.0 eV.[25] CasaXPS (version 2.3.16) was used for this purpose. SEM, XRD, and micro-Raman studies were conducted as previously reported.[23,26] The WITec micro-Raman spectrometer was used in this study, and a 532 nm laser served as the excitation source. A monochromator with a 1200 groove·mm^{-1} grating was used to disperse the scattered light and afterward focused onto a charge-coupled detector (CCD, Wright Instruments, Ltd.). Before all investigations, this equipment was calibrated using a Si wafer.

For transmission electron microscopy (TEM) investigation, the functionalized ZnO:Eu nanowires were scratched from the FTO substrate onto a lacey-carbon copper grid. The structural and chemical investigations were performed on an FEI Tecnai F30 microscope. Energy-dispersive X-ray spectroscopy (EDS) was enabled using an EDAX Si−Li drift detector for chemical species identification and elemental mapping. In addition, the energy-filtered (EF) TEM technique was applied for elemental imaging of europium species using the Eu(N)-edge at 143 eV. Electron energy-loss spectroscopy (EELS) was involved in the determination of the Eu oxidation state by collecting the energy-loss signals of the $N_{4,5}$-edge at 143 eV and $M_{4,5}$-edge around 1130 eV, respectively. Background subtraction was performed using the EELS plug-in implemented in the *DigitalMicrograph* software. The individual spectra were adjusted by an energy shift according to the shift of the zero-loss peak (ZLP) acquired before each measurement. The spectra were recorded with an energy resolution of 1.8 eV (half-width of the ZLP).

Samples with different europium contents were prepared by an electrochemical growth process at 80 °C, and micro-nanodevices were prepared by maskless nanoscale deposition in the focused electron/ion beam instrument (FEI, Helios Nanolab). In particular, a single ZnO:Eu nanowire was integrated into a device with two prepatterned electrodes, Si/SiO$_2$ and quartz with Cr/Au pads, as contact electrodes, as previously reported.[27,28] The study of the electrical current of a nanosensor based on a single ZnO:Eu nanowire was investigated using a two-point probe. By controlling the electrical current in the developed device, the electrical conductivity was studied in the environment and by exposing the nanosensor to a test gas. The nanosensors were tested at operating temperatures ranging from room temperature (RT) to 175 °C to observe the effect of this parameter on UV and gas detection performances. All nanosensors were tested at a relative humidity of 10% in the test chamber, and the effect of humidity was investigated by increasing the humidity to 50% RH. ZnO:Eu3 nanosensors were tested in dual-mode to see clear detection of H_2 gas during continuous UV light pulse.
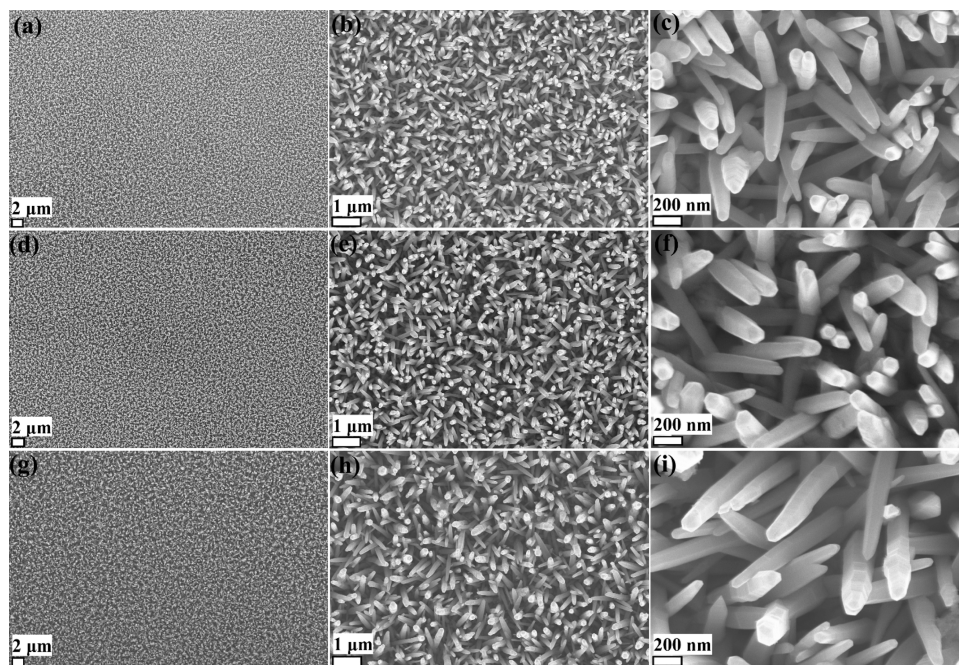
Figure 1. SEM images of ZnO:Eu nanowire arrays grown in electrolyte solution with $EuCl_3$ concentrations of (a–c) −3 μM, (d–f) −5 μM, and (g–i) −10 μM. The magnification increases from left to right.

We have performed DFT simulations, employing the generalized gradient approximation (GGA) within the PBE (Perdew–Burke–Ernzerhof)[29] exchange-correlation functional and the projected augmented wave (PAW) approach,[30,31] as implemented in the Vienna *ab initio* simulation package (VASP).[32] We have used the ZnO bulk and subsequent surface structures from previous works[27,33,34] as a starting model to investigate gas sensing, where the ZnO bulk unit cell structure was optimized using a 5 × 5 × 4 Monkhorst–Pack k point mesh.[35] The 4 × 4 supercell of the ZnO ($10\bar{1}0$) surfaces was modeled using a 3 × 3 × 1 Monkhorst–Pack k point mesh. The DFT-D3 approach as described by Grimme et al.[36] and implemented in VASP was employed to incorporate the long-range dispersion corrections while investigating gas molecule interactions. Other details remain the same as described in our earlier works.[27,33,34]

The adsorption energy of the H_2 molecule was computed as follows:

$$E_{ads} = E_{Complex} - (E_{Surf} + E_{Mol}) \tag{1}$$

where $E_{Complex}$ is the total energy of the surface with the molecule, E_{Surf} is the energy of the surface slab without the molecule, and E_{Mol} is the energy of the isolated molecule. E_{Mol} was calculated by modeling the isolated molecule in the center of a broken symmetry cell with lattice constants of 20 Å, inspecting only the gamma point of the Brillouin zone with the same accuracy parameters as employed for the surface's structures. Bader charges were calculated using the method developed by Henkelman and co-workers.[37]

3. RESULTS AND DISCUSSION

3.1. Morphological and Structural Characteristics.

Figure 1 presents SEM images at different magnifications showing the morphology of the synthesized ZnO:Eu nanowire arrays, namely, ZnO:Eu3, ZnO:Eu5, and ZnO:Eu10 sample sets. The low magnification images (Figure 1a,d,g) indicate a complete and homogeneous coverage of the FTO substrate by nanowire arrays, which exhibit highly uniform wires with even distribution in length and diameter, as evidenced by the high magnification images (Figure 1b,e,h). There are no significant differences in the nanowire morphologies with respect to the

increased concentration of $EuCl_3$ in the deposition electrolyte (Figure 1c,f,i). Individual nanowires were then incorporated into the nanosensor device using an FIB-SEM technique described in previous works.[38,39] Each nanowire was connected to contact pad Au electrodes by the deposition of a Pt line from a Pt-containing precursor using the metallic maskless deposition in a focused electron/ion beam system. The selected nanowires possess comparable high aspect ratios with a diameter of ∼90 nm and a length of ∼1.6 μm (see Figure 7a).

The crystal structure and crystal orientation of the ZnO:Eu nanowire arrays grown on the FTO/glass substrates were investigated by X-ray diffraction (XRD). Figure 2 shows the XRD patterns of ZnO:Eu6 and ZnO:Eu10. The reflections of the ZnO lattice can be indexed to the hexagonal wurtzite-type
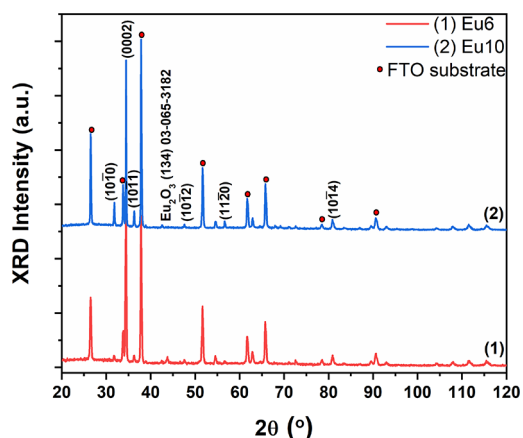

Figure 2. XRD pattern of ZnO:Eu nanowires grown by electrochemical deposition with different Eu concentrations: 6 and 10 μM $EuCl_3$ content in the electrolyte (samples: ZnO:Eu6 and ZnO:Eu10). Peaks from the used FTO substrate (SnO_2:F) are indicated by red circles.
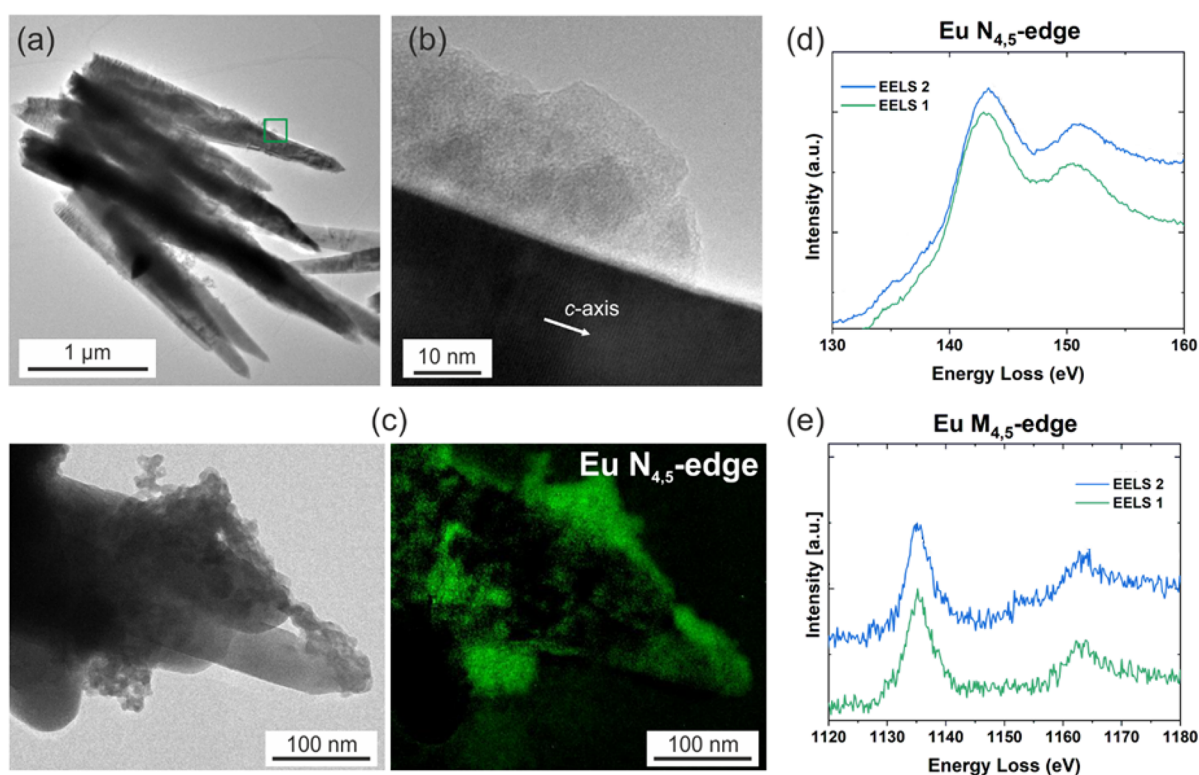
Figure 3. (a) TEM image of needle-shaped ZnO:Eu nanowires decorated with amorphous Eu-oxide species. (b) High-magnification micrograph showing the amorphous network covering the surface of the single crystalline ZnO nanowire. (c) Zero energy-loss filtered and EFTEM image recorded using the Eu $N_{4,5}$-edge. Electron energy-loss spectra recorded on Eu-networks intendity the fingerprint of Eu^{3+} according to the (d) $N_{4,5}$ and (e) $M_{4,5}$-edges.

structure according to the standard card (PDF 036-1451). One single Eu_2O_3 reflection was detected at 42.47° for ZnO:Eu6 and ZnO:Eu10, attributed to the cubic phase, according to PDF 03-065-3182. FTO substrate reflections have been attributed and are marked with the red circle in Figure 2. The nanowires are preferentially oriented along the *c*-axis direction, shown by the high-intensity reflection at 34.42° for the (0 0 0 2) plane of ZnO. Further, the good signal to noise ratio of the ZnO reflections indicate high crystallinity of the samples.[24]

TEM measurements (see Figure 3 and Figure S1) on the ZnO:Eu10 nanowires (10 μM) show uniform dimensions with lengths of 1.5−2 μm and diameters of 150−300 nm. Their crystalline structure was determined by high-resolution (HRTEM) imaging and electron diffraction (see Figure 3b and Figure S1). HRTEM imaging further evidences a network of dominantly amorphous particles, which partially covers the nanowires. Spectroscopic analysis on these agglomerates using EDS (see Figure S1) and EFTEM imaging (see Figure 3c) reveals Eu-containing species, associated with further content of silicon from the substrate and oxygen.

The valence state of Eu in the agglomerates is determined by analysis of the characteristic energy-losses of the inelastic scattered transmitted electrons.[40−43] The oxidation states of Eu^{2+} and Eu^{3+} are distinguishable either by a 2.5 eV energy shift of the characteristic $N_{4,5}$ and $M_{4,5}$ main core-loss features located at 143 and 1131 eV or by the shape of the $N_{4,5}$-edge featuring a double peak in the case of Eu^{3+} ions.

The EELS fine structure analysis is presented in Figure 3d,e showing the distinct fingerprints of the $N_{4,5}$- and $M_{4,5}$-edges matching to Eu^{3+} as in Eu_2O_3 (for further comparison we refer

to ref 42. Two representative measurements with STEM EELS identify the spectral signatures of Eu^{3+} at energy-loss features of 143.6 and 1136 eV. The deviation on the energy scale of 0.6 and 5 eV with respect to the reference values are rationalized by the position instability of the ZLP during the measurement.

In summary, analytical TEM studies reveal the surface functionalization or surface deposition of ZnO nanowires with amorphous networks containing Eu^{3+} ions and provide evidence for the formation of Eu_2O_3 in these agglomerates. Shallow doping of the ZnO lattice with Eu^{3+} during growth was not possible to determine either by superposition of signals from the agglomerates or the limited resolution of the spectroscopic methods to reliably trace element concentrations below 2 at. %.

3.2. Chemical Properties. To further investigate the possibility of Eu mixing and the Eu content or concentration, XPS measurements were performed for chemical identification to determine the molecular formula, chemical state, and electronic state of the elements present in a sample. The overview spectrum of the ZnO:Eu nanowire arrays is shown in Figure 4a and indicates the presence of Zn, Eu, O, and C, as well as Sn (in the case of samples ZnO:Eu3, ZnO:Eu6, and ZnO:Eu10). The signal of C originates from residual amounts of adventitious carbon and surface adsorbates such as atmospheric carbohydrates.[44,45] The presence of Sn is due to the use of FTO glass as substrate material for electro-deposition. For a detailed comparison, the C 1s, Zn 2p3/2, and Eu 3d5/2 lines are shown in Figure 4b. The different level of mixing in the different samples reflects on the europium signal, or content/concentration level. Accordingly, the corresponding Eu-3d5/2 line is the strongest for the ZnO:Eu10 sample and
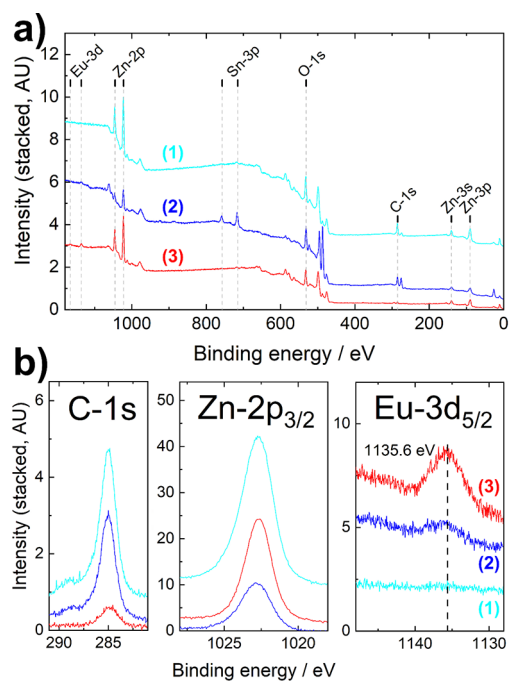
Figure 4. XPS spectra of ZnO:Eu nanowire samples: (a) overview spectrum indicating the presence of Eu, Zn, O, and C; (b) high resolution spectra of the C 1s line, Zn $2p_{3/2}$ line, and Eu $3d_{5/2}$ line. (1) 3, (2) 6, and (3) 10 μM $EuCl_3$ content in the electrolyte.
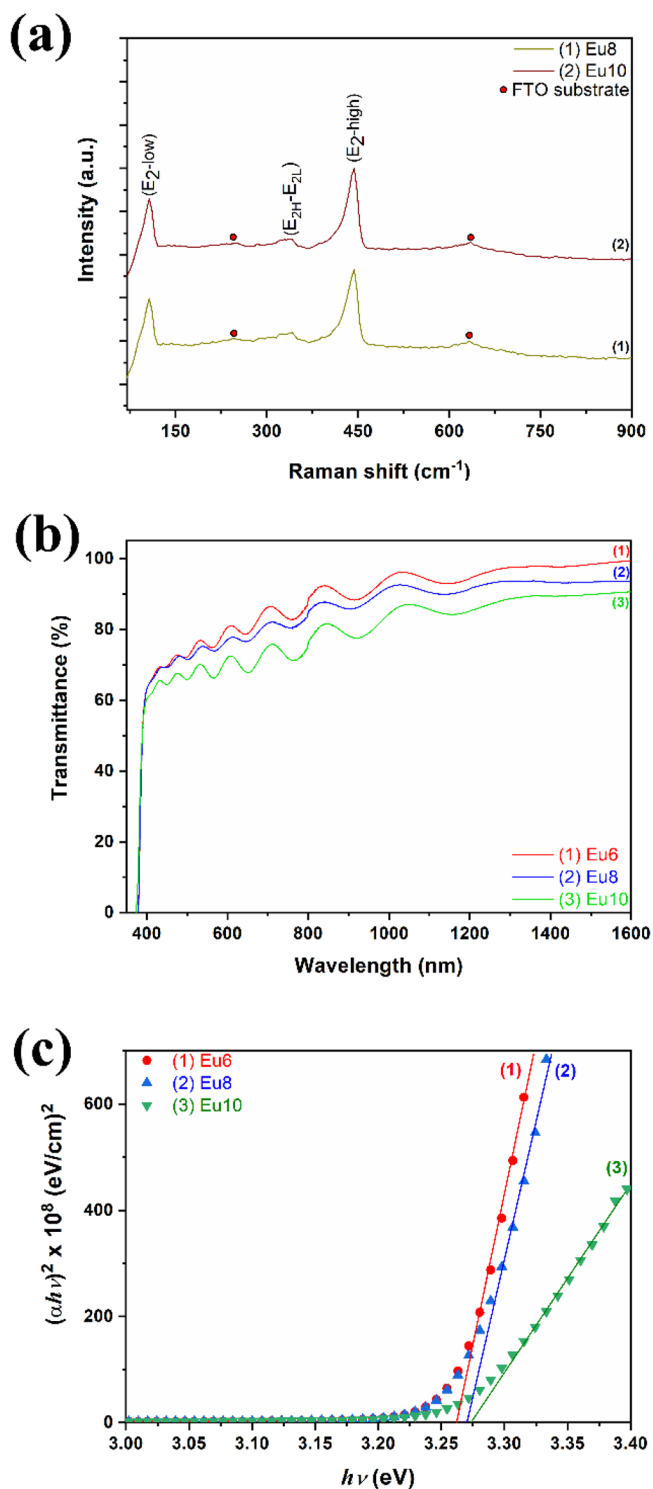

Figure 5. (a) Raman spectra of ZnO:Eu nanowires deposited with different Eu contents: (1) 8 and (2) 10 μM. (b) Transmission spectra of ZnO:Eu nanowires with different Eu contents: (1) 6, (2) 8, and (3) 10 μM. (c) Plot of $(\alpha h\nu)^2$ vs $(h\nu)$ for ZnO:Eu nanowires with different Eu contents: (1) 6, (2) 8, and (3) 10 μM.

the lowest for the ZnO:Eu3 sample. The position of the Eu-3d5/2 line is centered around 1135.6 eV, which corresponds well with Eu^{3+} in Eu_2O_3.[46] To indicate the europium concentration level, an exemplary quantification was conducted for the ZnO:Eu10 sample. The quantification of the ZnO:Eu nanowire arrays was performed based on the Zn-$2p_{3/2}$ and Eu-$3d_{5/2}$ lines (Figure 4b) for the sample with 10 μM, which showed the highest Eu signal. The Eu/Zn ratio in this XPS spectra quantification is 4/96, which relates to a concentration of europium of roughly 4%.

3.3. Raman Spectroscopy. Micro-Raman spectroscopy provides detailed structural data on the electrodeposited material, especially on the nanowire array vibrational properties, material quality, and phase. These are important to understand the transport properties and phonon interaction with the free charge carriers to determine the nanodevice performance. Several spectra of samples and different locations on the FTO substrate were measured, observing no significant difference. A typical spectrum corresponding to one position on the ZnO:Eu nanowire array is presented. The micro-Raman spectra of two samples with different Eu contents (ZnO:Eu8 and ZnO:Eu10) are illustrated in Figure 5a. Peaks of the FTO layer at 633 cm^{-1} were found in all samples. All other micro-Raman modes agree with the results for ZnO. The Raman modes for such a material can be represented as follows $\Gamma_{opt} = 1A_1 + 2B_1 + 1E_1 + 2E_2$. The mode at the 100 cm^{-1} (E_2-low) is attributed to the vibration of the Zn sub-lattice, while the peak at the 438 cm^{-1} (E_2-high) is related to the vibration of the oxygen atoms.[47] E_2-high is attributed to the ZnO nonpolar optical phonons of E_2 mode, which is one of the characteristic peaks of wurtzite ZnO with good-quality crystals.[47] A more detailed discussion can be found in a previous work.[24] Thus, the micro-Raman spectroscopy study confirms the good

crystalline quality of the nanowires observed in the XRD diffractogram.

3.4. Optical Properties. The optical properties of ZnO:Eu nanowire arrays with different concentrations of Eu were studied in the wavelength 300−1700 nm. The results are shown in Figure 5b, where optical transmittance values for

ZnO:Eu6, ZnO:Eu8, and ZnO:Eu10 are shown in percentage values from the reference sample. A decrease in optical transmission was observed with the increase in Eu content, as reported before.[23] It was observed that in the visible spectrum, optical transmission values are higher than 65%, while in the near-infrared spectrum, they are about 85%.

By extrapolating the linear segment of $(\alpha h\nu)^2$ versus photon energy $(h\nu)$, represented in Figure 5c, the optical band gap of ZnO:Eu nanowire arrays with different Eu contents was studied. A slight increase was observed with the increase in Eu content, from 3.26 eV for ZnO:Eu6 to 3.27 eV for ZnO:Eu10. These results show that the Eu content in ZnO does not affect significantly the optical band value, which was also observed in other studies.[23]

3.5. Gas Sensing Properties. To determine the response, selectivity, and behavior of a single nanowire ZnO:Eu compared to reference ZnO, the electrical response was recorded for different samples and the sensor was inserted into a measurement device. The electrical properties of the single ZnO:Eu nanowire have a significant effect on the response of the gas sensor to H₂ gas. The measurements were performed in the temperature range between 20 and 175 °C. The gas sensor properties of the ZnO:Eu-based sensors are investigated under the influence of different test gases, such as acetone, 2-butanol, ethanol, hydrogen, ammonia, n-propanol, and methane. Here, the gas response (S_g) to the target gas was determined using the ratio of electrical current through the sensor at gas exposure (I_{gas}) and I_{air} represents electrical current in air exposure.

$$S_g = \frac{I_{gas}}{I_{air}} \tag{2}$$

The dynamic response to 100 ppm H₂ gas at room temperature (RT) is represented in Figure 6a, showing a gas response of only $S_g = 2.1$ for the sample prepared with 5 μM europium chloride in bath (ZnO:Eu5). The response time represents the time it takes for the sensor to reach 90% of the maximum current after gas exposure. The recovery time represents the time it takes for the sensor to reach 10% of the initial current after stopping the gas exposure. The sample tested demonstrated reasonable response and recovery times at ~7 and ~42 s, respectively.

In addition, the sensor showed selectivity to hydrogen gas at room temperature with a response of 2.1 (Figure 6b) for the ZnO:Eu5 sample.

In Table 1 is the compared hydrogen gas response for sensors based on ZnO and doped/mixed ZnO; observing that by using ZnO:Eu nanowire-based nanosensors, we obtained a higher response at room temperature for a lower concentration of hydrogen (100 ppm) compared to a previously reported sensor based on Pd nanoparticles decorated on ZnO nanorods with a gas response of $S_g = 1.9$ for 1000 ppm hydrogen at room temperature.[48]

In addition, a proof-of-concept study measured the dynamic response of the sensor current to UV light at room temperature, and the properties upon UV light irradiation are shown in Figure S2a for the ZnO:Eu5 sample set. Here, a response time of ~28 and ~10 s for the recovery time were observed. The response time to UV is higher than that to hydrogen, while it recovers faster from UV exposure back to the baseline. Long response times to UV light can be explained by a gradual accumulation of unpaired electrons on the
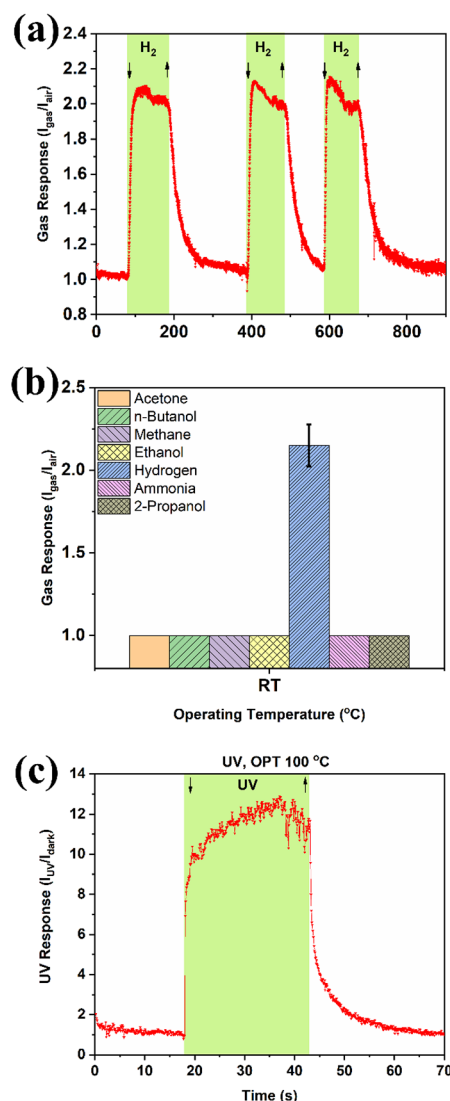
Figure 6. (a) Dynamic response of the ZnO:Eu5 nanosensor to 100 ppm of hydrogen gas at room temperature. (b) Gas response of the ZnO:Eu5 nanosensor to 100 ppm of various gases at room temperature. (c) UV response for the ZnO:Eu5 nanosensor at 100 °C operating temperature.

nanosensor surface until the desorption and re-adsorption of oxygen reach an equilibrium state.[50] The recovery time is caused by the quick recombination of holes with electrons when the UV light is switched off.[50]

The UV response (S_{UV}) was determined using the ratio

$$S_{UV} = \frac{I_{UV}}{I_{dark}} \tag{3}$$

where I_{UV} is the electrical current through the sensor at UV light exposure and I_{dark} represents the electrical current without UV light exposure.

The dynamic response to UV light at an operating temperature of 100 °C is shown in Figure 6c, where sensor ZnO:Eu5 showed a higher response than at room temperature to a UV light of ~12.8, with faster response and recovery times of ~8 and ~7 s, respectively.

In Figure 7c and Figure S3, the gas response to a series of different gases are shown and compared. From operating temperatures of 100 to 175 °C, a response and selectivity to

Table 1. Comparison of Response Value of Hydrogen Gas Sensor Using Zinc Oxide and Doped/Mixed Zinc Oxide Nanostructures
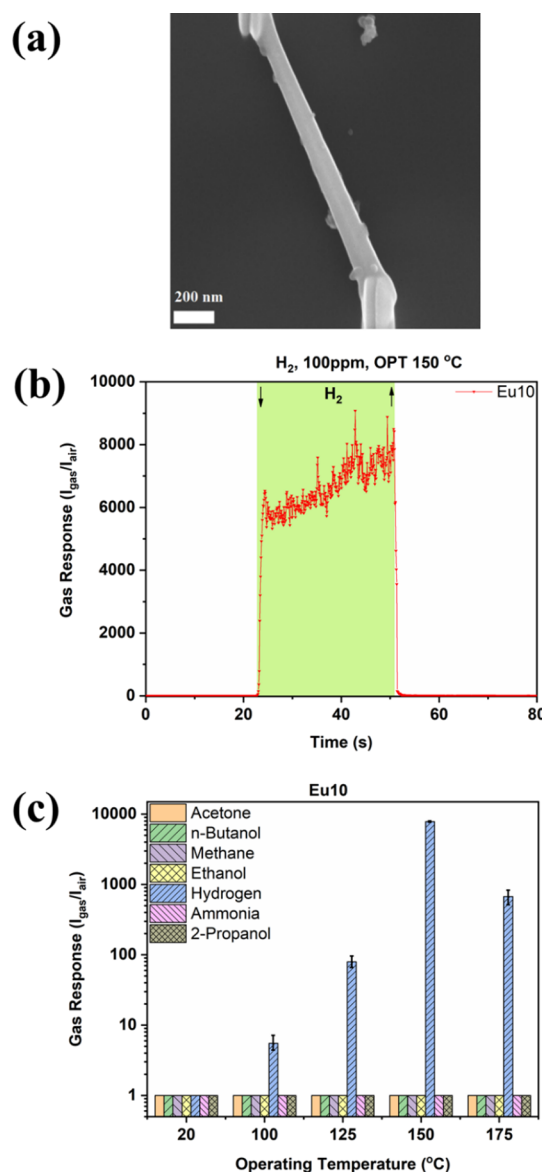
study	nanostructure	operating temperature	hydrogen concentration (ppm)	response value (S_g)
this work	ZnO:Eu5 nanowire	RT	100	2.1
this work	ZnO:Eu20 nanowire	100 °C	100	865
this work	ZnO:Eu20 nanowire	125 °C	100	672
this work	ZnO:Eu10 nanowire	150 °C	100	7860
this work	ZnO:Eu6 nanowire	175 °C	100	1607
Lupan et al.[23]	Pd-functionalized ZnO:Eu films	250 °C	100	115
Rashid et al.[48]	ZnO nanorod decorated with Pd nanoparticles	RT	1000	1.9
Kohlmann et al.[26]	ZnO nanobrush	100 °C	100	25
Kohlmann et al.[26]	ZnO nanobrush	125 °C	100	62
Kohlmann et al.[26]	ZnO nanobrush	150 °C	100	148
Khan et al.[49]	ZnO single nanowire	200 °C	100	2.5
Khan et al.[49]	ZnO multiple nanowires	200 °C	100	5.3

100 ppm hydrogen gas for all mixing concentrations of Eu were observed. All samples showed a gas response starting at 100 °C, increasing with increasing temperature up to 150 °C, and then decreasing, except for the ZnO:Eu6 sample (see Figure S3a). The maximum response of ∼7860 was achieved at 150 °C for the ZnO:Eu10 sample (see Figure 7b), dropping to ∼675 at 175 °C. The response time for the ZnO:Eu10 nanosensor at 150 °C was ∼17 s, while the recovery time was less than half a second.

The ZnO:Eu3 nanosensor was exposed to UV light and hydrogen gas at the same time to observe the influence on the sensing performance as a dual-mode sensor. In Figure S2b, the nanosensor was exposed continuously for ∼27 s to 100 ppm hydrogen gas and only for ∼10 s to UV light simultaneously. It was observed that the hydrogen response value of ∼44 was not influenced by the UV light applied in the middle of H$_2$ gas pulse.

However, in Figure S2c, the ZnO:Eu3 nanosensor was exposed continuously for ∼26 s to UV light and only for ∼10 s to 100 ppm hydrogen. It was observed that after applying hydrogen gas, the response value increased from ∼11 to ∼28, marked in the middle of the pulse overlapping, in Figure S2c. After stopping hydrogen gas, the response value decreased to ∼13, which is almost same value obtained under UV irradiation. Thus, we demonstrated dual-mode nanosensor to detect UV/H$_2$ light/gas simultaneously for selective detection of H$_2$ gas during UV irradiation and contribute to study its effect on the sensing mechanism.

These results can be explained by the fact that the nanosensor has a higher response value to hydrogen gas of ∼48 for this doping concentration, while the one for UV light is lower, meaning that during UV light exposure, the response

Figure 7. (a) SEM of the sensor based on the sample for ZnO:Eu10 (10 μM EuCl$_3$ content in the electrolyte); (b) gas response for 100 ppm hydrogen of a ZnO:Eu10 nanosensor at 150 °C operating temperature; (c) gas response for 100 ppm of different gases at 20, 100, 125, 150, and 175 °C operating temperatures for the ZnO:Eu10 nanosensor.

value is influenced by the hydrogen gas, until it reaches saturation.

When ZnO:Eu nanowires are exposed to UV light, photogenerated electron−hole pairs are created, affecting the chemisorption and desorption processes that take place on the surface of the nanosensor during hydrogen gas exposure.[51] However, applying H$_2$ gas pulse in the middle or simultaneously with a UV light, it can suggest that hydrogen interacts with adsorbed oxygen species on the surface of ZnO:Eu. Thus, it contributes to the sensing mechanism and the development of a dual-mode nanosensor. This concentration of ZnO:Eu3 was selected because its effect was more clearly observed and the response values are comparable.

Figure 8 shows a comparison of hydrogen gas response values at an operating temperature of 150 °C for ZnO:Eu samples with different Eu contents. It was observed that the
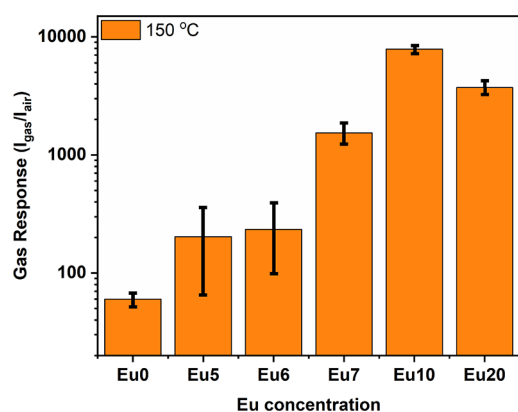
Figure 8. Gas response for 100 ppm hydrogen at 150 °C operating temperature for ZnO:Eu nanowires with different Eu contents: (1) 0, (2) 5, (3) 6, (4) 7, (5) 10, and (6) 20 μM EuCl$_3$ concentration in the electrolyte.

response value increased with the increase in Eu content in the samples, from ∼60 for the undoped ZnO:Eu0 up to ∼7860 for surface deposited ZnO:Eu10, and then decreased to ∼3725 for ZnO:Eu20. These results can be explained by the energy difference needed for activation, meaning that samples with different Eu contents and operating temperatures directly influence the sensor properties.

To verify the stability and repeatability of the ZnO:Eu20 nanosensor at 100 ppm hydrogen gas, a nanosensor was tested after 10 months, with the results shown in Figure S4. Initially, the maximum response value was ∼3725 at 150 °C, but after 10 months, the response value decreased to ∼900 at the same operating temperature. In contrast, it was observed that after 10 months, the response values strongly increased at the other operating temperatures of 100, 125, and 175 °C when compared to the data presented in Figure S3c. For example, at 100 °C, the gas response value increased from ∼5.5 to ∼865. The increase at lower operating temperatures could be explained by temperature-induced changes in the nanomaterial or contacts after the initial measurements, where the nanosensor was heated up to 175 °C, which may act as a thermal treatment that strongly affects the structures of the nanosensor and reduces some defects on the surface of the material. These findings indicate that a short annealing step of the ZnO:Eu nanosensors strongly benefits the gas sensing properties toward room temperature sensing with a high gas response.

In addition, 10 months after the initial measurements, the influence of relative humidity (RH%) on sensor performance was also investigated, since moisture is present in almost every practical application. Therefore, the ZnO:Eu20-based nanosensor was tested to 100 ppm hydrogen at different RH% values measured at 10 and 50% and at different operating temperatures (see Figure S5). The maximum response of ∼900 was achieved under conditions of 10% RH and an operating temperature of 150 °C. At an RH of 50% the maximum response decreased significantly to ∼200 (at 125 °C). At all operating temperatures, the response value was higher at lower RH%, showing an increase by a factor of 3.5−8, which indicates that the humidity lowers the sensor's response values.

The sensing mechanism of the nanosensors based on ZnO:Eu nanowires can be explained by an adsorption–desorption process that takes place on the surface between the target gas and nanomaterial,[52,53] producing a reversible
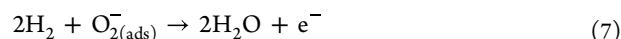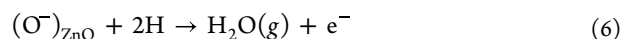
modification of the nanosensor parameters, for example, electrical resistance.[38,54]

At different operating temperatures, different oxygen species are adsorbed on the ZnO:Eu surface,[52,53] so when we obtain a response at an operating temperature under 150 °C, interaction takes place between molecular oxygen O$_2^-$ and the target gas.[52−54] At operating temperatures above 150 °C, interaction takes place between atomic oxygen species O$^-$ and O^{2-} and the target gas. Interactions between oxygen and the target gas can be summarized by the following reactions:[38]

$$O_2(gas) \leftrightarrow O_2(ads) \tag{4}$$

$$O_2(ads) + e^- \leftrightarrow O_2^-(ads) \tag{5}$$

Since we observed a selectivity to 100 ppm hydrogen gas, the detection mechanism will be based on the interaction between hydrogen and oxygen species adsorbed on the surface of the ZnO:Eu nanowire and the Eu$_2$O$_3$ nanoparticles on its surface. After applying hydrogen, which is a reductive gas, the nanosensor based on an *n*-type material will decrease its electrical resistance and increase its current, as shown in sensor measurements (see Figures 6a and 7b).

At room temperature, interactions that take place can be summed up by the following reactions:[38,54]

$$(O^-)_{ZnO} + 2H \rightarrow H_2O(g) + e^- \tag{6}$$

$$2H_2 + O_{2(ads)}^- \rightarrow 2H_2O + e^- \tag{7}$$

After the hydrogen gas is removed, the electrical resistance returns to its initial level after some time.

Mixing ZnO with surface-deposited Eu results in electrical charge transfer between Zn^{2+} and Eu^{3+} with increasing Eu concentration, which changes the electronic properties of Zn, such as changing the electric field and increasing the electron density,[23] observing a tendency of an increase of initial electrical resistance at room temperatures for nanosensors with different Eu concentrations, as shown in Figure S6. The enhanced hydrogen response of ZnO:Eu compared to ZnO may be due to this electrical charge transfer, which leads to a higher coverage of the surface with oxygen species due to a higher number of free electrons.[23]

3.6. DFT Modeling: ZnO:Eu Surface−H$_2$ Gas Molecule Interaction. As described in the *Computational* section 2, we started with our earlier surface models,[27] considering the most stable termination of the ZnO (10$\bar{1}$0) surface (shown in Figure S7 and described in Text S1), based on the calculated surface energies from our earlier work[27] and other works in the literature.[55,56] The slab comprised a total of six atomic layers, where the atomic coordinates of the bottom four layers were frozen at their bulk positions. We first investigated H$_2$ gas molecule interaction with the ZnO (10$\bar{1}$0) surface and found that the molecule interacts very weakly with no direct bond between the surface and molecule. The hydrogen molecule exhibits physisorption with an interaction energy of −21.3 kJ/mol. This is similar to our earlier work employing the DFT-D2 approach,[57] where very weak interaction was found with an interaction energy of −24.9 kJ/mol.[27] This small variation in interaction energy values is due to the different levels of dispersion correction functional used in the present work.[36]

Further, in order to model ZnO:Eu structures, we started from a 4 × 4 supercell of the ZnO (10$\bar{1}$0) surface replacing the most exposed surface Zn atom with a Eu atom. Here, we note that the Eu atom bonds to three surface oxygen atoms in the

same top layer (bond lengths varying from 2.22 to 2.69 Å) and one oxygen atom in the second layer beneath (Figure S8). This was the most stable having the lowest ground state energy,[27] compared to Eu doping on other surface sites in the top surface layer or sub-surface layers. Next, we investigated the interaction of an H_2 gas molecule with this single atom Eu in the ZnO:Eu ($10\bar{1}0$) surface by placing the molecule in different initial orientations to the surface and exploring different surface adsorption sites. We note that the H_2 molecule shows weak interaction with the surface, with one of the hydrogen atoms forming a weak bond with the surface oxygen atom having a bond length of H−O = 2.31 Å (Figure 9a). As a result of the surface oxygen atom interacting with the
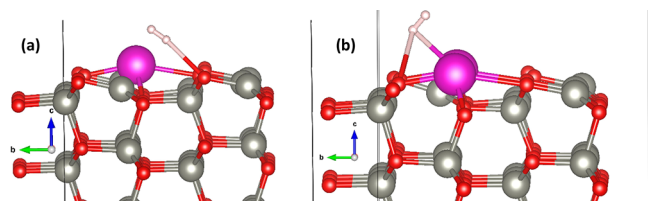

Figure 10. (a) Charge density difference plot iso-surfaces of the H_2 molecule interaction at the Eu_2:ZnO ($10\bar{1}0$) surface, where the H_2 molecule gains 0.22 e^- in Bader charge. Blue and yellow colored iso-surfaces indicate negative and positive changes in charges, respectively. (b) H_2O and H_2 molecules over the Eu_2:ZnO ($10\bar{1}0$) surface.

Figure 9. DFT relaxed structure of one H_2 molecule at (a) the Eu:ZnO($10\bar{1}0$) surface and (b) the Eu_2:ZnO($10\bar{1}0$) surface. O, Zn, and Eu atoms are denoted by red-, gray-, and purple-colored balls, respectively, while small pink-colored balls denote H atoms.

H_2 molecule, the Zn−O bond length increases from 1.94 to 1.95 Å, as this the oxygen atom moves upward to bind the H_2 molecule, with a binding energy of −28.94 kJ/mol.

In order to investigate the presence of more Eu atoms on the surface, we further doped the ZnO:Eu surface with one more Eu atom by replacing another nearby exposed surface Zn atom to mimic the formation of a $ZnO:Eu_2O_3$ surface. Surface rearrangement takes place where each substituted Eu atom bonds to four nearby oxygen atoms with bond lengths varying from 2.21 to 2.76 Å (Figure S9). In order to further investigate the surface−H_2 interaction, we placed a H_2 molecule close to the Eu atoms in different orientations and observed that the H_2 molecule binds comparatively stronger with this surface. One of the hydrogen atoms interacts with two surface oxygen atoms, at distances of 2.39 and 2.89 Å (Figure 9b). The surface Eu atom also moves upward to bind the H_2 molecule at a distance of 2.72 Å. As a result of this Eu−H_2 molecule interaction, the surface Eu−O bonds elongate and the bond length of the Eu atom with the sublayer oxygen atom increases from 2.21 to 2.22 Å, as oxygen atoms move to bind with the H_2 molecule. The presence of two Eu atoms in the ZnO ($10\bar{1}0$) surface results in comparatively better interaction of the H_2 molecule with the surface due to the presence of more valence electrons, thereby increasing the activity of the surface with an interaction energy of −30 kJ/mol. The surface−H_2 molecule interaction is reflected in our charge density difference plot as well, where we note significant charge redistribution, as the surface oxygen atom loses electrons (Bader charge −1.20 e^-), while the Eu atom gains electrons (Bader charge 1.36 e^-), as denoted in Figure 10a by yellow- and blue-colored iso-surfaces, respectively. The H_2 interaction is also reflected in terms of changes in the Fermi energy, as E_F shifts to −1.59 from −1.61 eV.

In order to investigate the effect of humidity, we next investigated the interaction of a water molecule with the Eu_2:ZnO surface with the pre-adsorbed H_2 molecule, where we found that as soon as the water molecule comes into contact
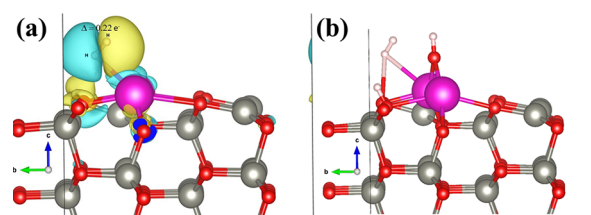
with the surface Eu atoms, it spontaneously dissociates into H and OH ions species. The H^+ ion bonds with a surface O atom, which is connected to a Eu atom, while the OH species binds the two Eu atoms, as shown in Figure 10b. As a result, the H_2 molecule now interacts comparatively weaker with the surface, increasing the H−O (hydrogen atom to surface oxygen atom) distance to 2.44 Å and the H−Eu distance to 2.81 Å. As such, we consider that in the presence of more water molecules, surface oxygen and Eu sites will become covered by water, thereby decreasing the sensitivity of the surface toward H_2 gas molecules.

4. CONCLUSIONS

In this study, the effects of Eu concentration in the electrolyte bath (ranging from 0 to 20 μM) on the morphology, structure, chemical, optical, electrical, and gas sensing characteristics of ZnO:Eu nanowires with good crystallinity are described. The addition of Eu (3−20 μM Eu ions in the electrolyte) and simultaneous functionalization of the surface with europium oxide agglomerates resulted in high selectivity and excellent sensitivity to hydrogen gas, leading to a maximum gas response of ∼7860 at 100 ppm H_2 and an operating temperature of 150 °C. DFT simulations also confirmed that Eu mixing concentration increases the activity of the ZnO surface, and the Eu-mixed material shows better sensitivity toward the H_2 gas. For the sample containing 5 μM Eu, both hydrogen and UV responses were detected even at room temperature, which is essential to detect the flame generated by a hydrogen−oxygen mixture. The combustion flames emit UV radiation, and the application requires the need to heat the sensor to be eliminated. We demonstrated a possibility for a new type of dual-mode nanosensor to detect UV/H_2 gas simultaneously for selective detection of H_2 during UV irradiation.

To test the nanosensor's ability to reliably detect hydrogen leaks in different environments, the effect of humidity on the sensing properties was investigated. A decrease in response to hydrogen by a factor of 3.5 to 8 was observed with 50% RH at different operating temperatures, but this sensor remained selective and sensitive. DFT simulations indicate that the H_2O molecule interacts with Eu sites on the ZnO surface, thereby lowering the interaction and sensitivity toward H_2 gas molecules.

Nanosensors based on ZnO:Eu nanowires have shown an increase in electrical conductivity upon exposure to H_2, demonstrating the n-type conductivity of the nanowires, which involves the formation of oxygen species that interact with the ZnO:Eu nanosensor surface.

The results obtained for a sensor based on a single ZnO:Eu nanowire can be used to further enhance the growth parameters, such as doping or mixing content, to enhance the response to hydrogen gas and UV radiation down to room temperature, to develop dual-mode nanosensors, and to integrate the material into devices for personal, industrial, safety, and environmental use.

■ ASSOCIATED CONTENT

ⓢ Supporting Information

The Supporting Information is available free of charge at https://pubs.acs.org/doi/10.1021/acsami.2c10975.

> TEM images of the ZnO:Eu nanowire showing its morphology at a large scale and higher magnification of one nanowire functionalized with a porous network coating of Eu_2O_3; compositional images measured by elemental EDX mapping at the microstructural level of ZnO:Eu deposition and EDX spectra; summary of the UV nanosensors based on ZnO:Eu5 and 100 ppm of hydrogen gas in air at different operating temperatures and RH%; response to UV light and 100 ppm hydrogen for the ZnO:Eu3 dual-mode nanosensor at 100 °C; gas response for 100 ppm of different gases at various operating temperatures for ZnO:Eu 6, 10, and 20; comparison of the gas response at different operating temperatures for the ZnO:Eu20 nanosensor; gas response for the ZnO:Eu20 nanosensor at two different relative humidities (RH%); comparison of initial electrical resistance for different Eu concentration nanosensors at room temperature; DFT modeling of ZnO and ZnO:Eu structures; relaxed structure of one and two Eu atoms doped in a ZnO $(10\bar{1}0)$ surface (PDF)

■ AUTHOR INFORMATION

Corresponding Authors

Cristian Lupan − *Center for Nanotechnology and Nanosensors, Department of Microelectronics and Biomedical Engineering, Faculty of Computers, Informatics and Microelectronics, Technical University of Moldova, MD-2004 Chisinau, Republic of Moldova*; Email: cristian.lupan@mib.utm.md

Abhishek Kumar Mishra − *Department of Physics, Applied Science Cluster, School of Engineering, University of Petroleum and Energy Studies (UPES), Energy Acres Building, Dehradun 248007 Uttrakhand, India*; Email: akmishra@ddn.upes.ac.in

Alexander Vahl − *Chair for Multicomponent Materials, Faculty of Engineering, Department of Materials Science, Kiel University, D-24143 Kiel, Germany*; Email: alva@tf.uni-kiel.de

Oleg Lupan − *Center for Nanotechnology and Nanosensors, Department of Microelectronics and Biomedical Engineering, Faculty of Computers, Informatics and Microelectronics, Technical University of Moldova, MD-2004 Chisinau, Republic of Moldova; Functional Nanomaterials, Faculty of Engineering, Department of Materials Science, Kiel University, D-24143 Kiel, Germany; PSL Université, Chimie ParisTech, CNRS, Institut de Recherche de Chimie Paris (IRCP), 75005 Paris, France; Department of Physics, University of Central Florida, Orlando, Florida 32816-2385,* United States; orcid.org/0000-0002-7913-9712; Email: ollu@tf.uni-kiel.de, oleg.lupan@mib.utm.md

Sandra Hansen − *Functional Nanomaterials, Faculty of Engineering, Department of Materials Science, Kiel University, D-24143 Kiel, Germany*; orcid.org/0000-0002-3529-8367; Email: sn@tf.uni-kiel.de

Authors

Niklas Wolff − *Chair for Synthesis and Real Structure, Faculty of Engineering, Department of Materials Science, Kiel University, D-24143 Kiel, Germany*

Jonas Drewes − *Chair for Multicomponent Materials, Faculty of Engineering, Department of Materials Science, Kiel University, D-24143 Kiel, Germany*; orcid.org/0000-0002-8539-1543

Helge Krüger − *Functional Nanomaterials, Faculty of Engineering, Department of Materials Science, Kiel University, D-24143 Kiel, Germany*; orcid.org/0000-0002-9638-8753

Thierry Pauporté − *PSL Université, Chimie ParisTech, CNRS, Institut de Recherche de Chimie Paris (IRCP), 75005 Paris, France*

Bruno Viana − *PSL Université, Chimie ParisTech, CNRS, Institut de Recherche de Chimie Paris (IRCP), 75005 Paris, France*

Lorenz Kienle − *Chair for Synthesis and Real Structure, Faculty of Engineering, Department of Materials Science, Kiel University, D-24143 Kiel, Germany*

Rainer Adelung − *Functional Nanomaterials, Faculty of Engineering, Department of Materials Science, Kiel University, D-24143 Kiel, Germany*; orcid.org/0000-0002-2617-678X

Nora H de Leeuw − *School of Chemistry, University of Leeds, Leeds LS2 9JT, United Kingdom; Department of Earth Sciences, Utrecht University, 3584 CB Utrecht, The Netherlands*; orcid.org/0000-0002-8271-0545

Complete contact information is available at:
https://pubs.acs.org/10.1021/acsami.2c10975

Author Contributions

The manuscript was written through contributions of all authors. All authors have given approval to the final version of the manuscript. C.L., Th.P., and O.L. carried out laboratory research and synthesized the ZnO:Eu nanomaterial. C.L., N.W., and J.D. wrote draft of the manuscript. N.W. and L.K. performed all TEM and EDS experiments and data analysis. J.D. and A.V. realized all XPS experiments and data analysis. C.L., O.L., and R.A. adapted the technological approach for material integration/fabrication of the sensors for gas detection and SEM−EDX FIB-SEM laboratory research. C.L. carried out laboratory research and the measurement of sensing properties of sensors based on such structures and analyzed all data. C.L., Th.P., B.V., and O.L. realized all optical experiments and data analysis. S.H., H.K., O.L., and R.A. did the study conception for battery safety application. C.L., N.W., Th.P., R.A., and A.V. analyzed the results, including experimental data and revised draft. C.L., N.W., A.V., H.K., and R.A. did the draft of the article. A.K.M. carried out DDTT calculations and together with N.H.d.L. drafted the computational part for the manuscript. C.L., S.H., Th.P., and R.A. did the study conception and design and gave final approval of the version to be published. All authors reviewed the manuscript.

■ REFERENCES

(1) Saeedmanesh, A.; Mac Kinnon, M. A.; Brouwer, J. Hydrogen Is Essential for Sustainability. *Curr. Opin. Electrochem.* **2018**, *12*, 166−181.

(2) Arshad, F.; Haq, T.; Hussain, I.; Sher, F. Recent Advances in Electrocatalysts toward Alcohol-Assisted, Energy-Saving Hydrogen Production. *ACS Appl. Energy Mater.* **2021**, *4*, 8685−8701.

(3) Ohsaki, T.; Kishi, T.; Kuboki, T.; Takami, N.; Shimura, N.; Sato, Y.; Sekino, M.; Satoh, A. Overcharge Reaction of Lithium-Ion Batteries. *J. Power Sources* **2005**, *146*, 97−100.

(4) Essl, C.; Golubkov, A. W.; Fuchs, A. Comparing Different Thermal Runaway Triggers for Two Automotive Lithium-Ion Battery Cell Types. *J. Electrochem. Soc.* **2020**, *167*, 130542.

(5) *Guide for the Ventilation and Thermal Management of Batteries for Stationary Applications*; IEEE, 2018.

(6) Chen, Y.; Kang, Y.; Zhao, Y.; Wang, L.; Liu, J.; Li, Y.; Liang, Z.; He, X.; Li, X.; Tavajohi, N.; Li, B. A Review of Lithium-Ion Battery Safety Concerns: The Issues, Strategies, and Testing Standards. *J. Energy Chem.* **2021**, *59*, 83−99.

(7) Sundén, B. Battery Technologies. *Hydrogen Batter. Fuel Cells* **2019**, 57−79.

(8) Hosseini, S. E.; Wahid, M. A. Hydrogen from Solar Energy, a Clean Energy Carrier from a Sustainable Source of Energy. *Int. J. Energy Res.* **2020**, *44*, 4110−4131.

(9) Essl, C.; Golubkov, A. W.; Gasser, E.; Nachtnebel, M.; Zankel, A.; Ewert, E.; Fuchs, A. Comprehensive Hazard Analysis of Failing Automotive Lithium-ion Batteries in Overtemperature Experiments. *Batteries* **2020**, *6*, 30.

(10) Golubkov, A. W.; Scheikl, S.; Planteu, R.; Voitic, G.; Wiltsche, H.; Stangl, C.; Fauler, G.; Thaler, A.; Hacker, V. Thermal Runaway of Commercial 18650 Li-Ion Batteries with LFP and NCA Cathodes - Impact of State of Charge and Overcharge. *RSC Adv.* **2015**, *5*, 57171−57186.

(11) International Code Council. *2018 International Fire Code*; International Code Council, 2017.

(12) Carcassi, M. N.; Fineschi, F. Deflagrations of H_2-Air and CH_4-Air Lean Mixtures in a Vented Multi-Compartment Environment. *Energy* **2005**, *30*, 1439−1451.

(13) Lupan, O.; Cretu, V.; Postica, V.; Ahmadi, M.; Cuenya, B. R.; Chow, L.; Tiginyanu, I.; Viana, B.; Pauporté, T.; Adelung, R. Silver-Doped Zinc Oxide Single Nanowire Multifunctional Nanosensor with a Significant Enhancement in Response. *Sens. Actuators, B* **2016**, *223*, 893−903.

(14) Gorup, L. F.; Amorin, L. H.; Camargo, E. R.; Sequinel, T.; Cincotto, F. H.; Biasotto, G.; Ramesar, N.; de La Porta, F. A. Methods for Design and Fabrication of Nanosensors: The Case of ZnO-Based Nanosensor. *Nanosensors Smart Cities* **2020**, 9−30.

(15) Hastir, A.; Kohli, N.; Singh, R. C. Comparative Study on Gas Sensing Properties of Rare Earth (Tb, Dy and Er) Doped ZnO Sensor. *J. Phys. Chem. Solids* **2017**, *105*, 23−34.

(16) Lupan, O.; Postica, V.; Pauporté, T.; Viana, B.; Terasa, M. I.; Adelung, R. Room Temperature Gas Nanosensors Based on Individual and Multiple Networked Au-Modified ZnO Nanowires. *Sens. Actuators, B* **2019**, *299*, 126977.

(17) Lupan, O.; Postica, V.; Wolff, N.; Su, J.; Labat, F.; Ciofini, I.; Cavers, H.; Adelung, R.; Polonskyi, O.; Faupel, F.; Kienle, L.; Viana, B.; Pauporté, T. Lowerature Solution Synthesis of Au-Modified ZnO Nanowires for Highly Efficient Hydrogen Nanosensors. *ACS Appl. Mater. Interfaces* **2019**, *11*, 32115−32126.

(18) Postica, V.; Vahl, A.; Santos-Carballal, D.; Dankwort, T.; Kienle, L.; Hoppe, M.; Cadi-Essadek, A.; De Leeuw, N. H.; Terasa, M. I.; Adelung, R.; Faupel, F.; Lupan, O. Tuning ZnO Sensors Reactivity toward Volatile Organic Compounds via Ag Doping and Nanoparticle Functionalization. *ACS Appl. Mater. Interfaces* **2019**, *11*, 31452−31466.

(19) Han, D.; Yang, J.; Gu, F.; Wang, Z. Effects of Rare Earth Element Doping on the Ethanol Gas-Sensing Performance of Three-Dimensionally Ordered Macroporous In_2O_3. *RSC Adv.* **2016**, *6*, 45085−45092.

(20) Dash, D.; Panda, N. R.; Sahu, D. Photoluminescence and Photocatalytic Properties of Europium Doped ZnO Nanoparticles. *Appl. Surf. Sci.* **2019**, *494*, 666−674.

(21) Pauporté, T.; Pellé, F.; Viana, B.; Aschehoug, P. Luminescence of Nanostructured Eu3+/ZnO Mixed Films Prepared by Electro-deposition. *J. Phys. Chem. C* **2007**, *111*, 15427−15432.

(22) Zhao, S.; Shen, Y.; Li, A.; Chen, Y.; Gao, S.; Liu, W.; Wei, D. Effects of Rare Earth Elements Doping on Gas Sensing Properties of ZnO Nanowires. *Ceram. Int.* **2021**, *47*, 24218−24226.

(23) Lupan, C.; Khaledialidusti, R.; Mishra, A. K.; Postica, V.; Terasa, M. I.; Magariu, N.; Pauporté, T.; Viana, B.; Drewes, J.; Vahl, A.; Faupel, F.; Adelung, R. Pd-Functionalized ZnO:Eu Columnar Films for Room-Temperature Hydrogen Gas Sensing: A Combined Experimental and Computational Approach. *ACS Appl. Mater. Interfaces* **2020**, *12*, 24951−24964.

(24) Lupan, O.; Pauporté, T.; Viana, B.; Aschehoug, P.; Ahmadi, M.; Cuenya, B. R.; Rudzevich, Y.; Lin, Y.; Chow, L. Eu-Doped ZnO Nanowire Arrays Grown by Electrodeposition. *Appl. Surf. Sci.* **2013**, *282*, 782−788.

(25) Moulder, J. F.; Stickle, W. F.; Sobol, P. E.; Bomben, K. D. *Handbook of Photoelectron Spectroscopy.* Phys. Electron. Inc.: Eden Prairie, Minnesota 1992.

(26) Kohlmann, N.; Hansen, L.; Lupan, C.; Schu, U.; Reimers, A.; Schu, F.; Adelung, R.; Kersten, H.; Kienle, L. Fabrication of ZnO Nanobrushes by H 2 − C 2 H 2 Plasma Etching for H 2 2 Sensing Applications. 2021, 13 (51), 61758−61769, DOI: 10.1021/acsami.1c18679.

(27) Lupan, O.; Magariu, N.; Khaledialidusti, R.; Mishra, A. K.; Hansen, S.; Krüger, H.; Postica, V.; Heinrich, H.; Viana, B.; Ono, L. K.; Cuenya, B. R.; Chow, L.; Adelung, R.; Pauporté, T. Comparison of Thermal Annealing versus Hydrothermal Treatment Effects on the Detection Performances of ZnO Nanowires. *ACS Appl. Mater. Interfaces* **2021**, *13*, 10537−10552.

(28) Lupan, O.; Chai, G.; Chow, L. Fabrication of ZnO Nanorod-Based Hydrogen Gas Nanosensor. *Microelectron. J.* **2007**, *38*, 1211−1216.

(29) Perdew, J. P.; Burke, K.; Ernzerhof, M. Generalized Gradient Approximation Made Simple. *Phys. Rev. Lett.* **1996**, *77*, 3865−3868.

(30) Blöchl, P. E. Projector Augmented-Wave Method. *Phys. Rev. B* **1994**, *50*, 17953−17979.

(31) Kresse, G.; Joubert, D. From Ultrasoft Pseudopotentials to the Projector Augmented-Wave Method. *Phys. Rev. B* **1999**, *59*, 11−1775.

(32) Kresse, G.; Furthmüller, J. Efficiency of Ab-Initio Total Energy Calculations for Metals and Semiconductors Using a Plane-Wave Basis Set. *Comput. Mater. Sci.* **1996**, *6*, 15−50.

(33) Postica, V.; Gröttrup, J.; Adelung, R.; Lupan, O.; Mishra, A. K.; de Leeuw, N. H.; Ababii, N.; Carreira, J. F. C.; Rodrigues, J.; Sedrine, N. B.; Correia, M. R.; Monteiro, T.; Sontea, V.; Mishra, Y. K. Multifunctional Materials: A Case Study of the Effects of Metal Doping on ZnO Tetrapods with Bismuth and Tin Oxides. *Adv. Funct. Mater.* **2017**, *27*, 1604676.

(34) Lupan, O.; Postica, V.; Gröttrup, J.; Mishra, A. K.; De Leeuw, N. H.; Carreira, J. F. C.; Rodrigues, J.; Ben Sedrine, N.; Correia, M. R.; Monteiro, T.; Cretu, V.; Tiginyanu, I.; Smazna, D.; Mishra, Y. K.; Adelung, R. Hybridization of Zinc Oxide Tetrapods for Selective Gas Sensing Applications. *ACS Appl. Mater. Interfaces* **2017**, *9*, 4084−4099.

(35) Pack, J. D.; Monkhorst, H. J. "Special Points for Brillouin-Zone Integrations"-a Reply. *Phys. Rev. B* **1977**, *16*, 1748−1749.

(36) Grimme, S.; Antony, J.; Ehrlich, S.; Krieg, H. A Consistent and Accurate Ab Initio Parametrization of Density Functional Dispersion Correction (DFT-D) for the 94 Elements H-Pu. *J. Chem. Phys.* **2010**, *132*, 154104.

(37) Henkelman, G.; Arnaldsson, A.; Jónsson, H. A Fast and Robust Algorithm for Bader Decomposition of Charge Density. *Comput. Mater. Sci.* **2006**, *36*, 354−360.

(38) Lupan, O.; Chai, G.; Chow, L. Novel Hydrogen Gas Sensor Based on Single ZnO Nanorod. *Microelectron. Eng.* **2008**, *85*, 2220−2225.

(39) Lupan, O.; Ursaki, V. V.; Chai, G.; Chow, L.; Emelchenko, G. A.; Tiginyanu, I. M.; Gruzintsev, A. N.; Redkin, A. N. Selective Hydrogen Gas Nanosensor Using Individual ZnO Nanowire with Fast Response at Room Temperature. *Sens. Actuators, B* **2010**, *144*, 56−66.

(40) Hocking, W. H.; Matthew, J. A. D. Electron Spectroscopy of Europium. *J. Phys. Condens. Matter.* **1990**, *2*, 3643−3658.

(41) Tizei, L. H. G.; Nakanishi, R.; Kitaura, R.; Shinohara, H.; Suenaga, K. Core-Level Spectroscopy to Probe the Oxidation State of Single Europium Atoms. *Phys. Rev. Lett.* **2015**, *114*, 197602.

(42) Mundy, J. A.; Hodash, D.; Melville, A.; Held, R.; Mairoser, T.; Muller, D. A.; Kourkoutis, L. F.; Schmehl, A.; Schlom, D. G. Hetero-Epitaxial EuO Interfaces Studied by Analytic Electron Microscopy. *Appl. Phys. Lett.* **2014**, *104*, No. 091601.

(43) Mairoser, T.; Mundy, J. A.; Melville, A.; Hodash, D.; Cueva, P.; Held, R.; Glavic, A.; Schubert, J.; Muller, D. A.; Schlom, D. G.; Schmehl, A. High-Quality EuO Thin Films the Easy Way via Topotactic Transformation. *Nat. Commun.* **2015**, *6*, 1−7.

(44) Postica, V.; Vahl, A.; Strobel, J.; Santos-Carballal, D.; Lupan, O.; Cadi-Essadek, A.; De Leeuw, N. H.; Schütt, F.; Polonskyi, O.; Strunskus, T.; Baum, M.; Kienle, L.; Adelung, R.; Faupel, F. Tuning Doping and Surface Functionalization of Columnar Oxide Films for Volatile Organic Compound Sensing: Experiments and Theory. *J. Mater. Chem. A* **2018**, *6*, 23669−23682.

(45) Lupan, O.; Emelchenko, G. A.; Ursaki, V. V.; Chai, G.; Redkin, A. N.; Gruzintsev, A. N.; Tiginyanu, I. M.; Chow, L.; Ono, L. K.; Roldan Cuenya, B.; Heinrich, H.; Yakimov, E. E. Synthesis and Characterization of ZnO Nanowires for Nanosensor Applications. *Mater. Res. Bull.* **2010**, *45*, 1026−1032.

(46) Rumble, J. R.; Bickham, D. M.; Powell, C. J. The NIST X-ray Photoelectron Spectroscopy Database. *Surf. Interface Anal.* **1992**, *19*, 241−246.

(47) Lupan, O.; Chai, G.; Chow, L.; Emelchenko, G. A.; Heinrich, H.; Ursaki, V. V.; Gruzintsev, A. N.; Tiginyanu, I. M.; Redkin, A. N. Ultraviolet Photoconductive Sensor Based on Single ZnO Nanowire. *Phys. Status Solidi Appl. Mater. Sci.* **2010**, *207*, 1735−1740.

(48) Rashid, T. R.; Phan, D. T.; Chung, G. S. A Flexible Hydrogen Sensor Based on Pd Nanoparticles Decorated ZnO Nanorods Grown on Polyimide Tape. *Sens. Actuators, B* **2013**, *185*, 777−784.

(49) Khan, R.; Ra, H. W.; Kim, J. T.; Jang, W. S.; Sharma, D.; Im, Y. H. Nanojunction Effects in Multiple ZnO Nanowire Gas Sensor. *Sens. Actuators, B* **2010**, *150*, 389−393.

(50) Zhou, J.; Gu, Y.; Hu, Y.; Mai, W.; Yeh, P. H.; Bao, G.; Sood, A. K.; Polla, D. L.; Wang, Z. L. Gigantic Enhancement in Response and Reset Time of ZnO UV Nanosensor by Utilizing Schottky Contact and Surface Functionalization. *Appl. Phys. Lett.* **2009**, *94*, 191103.

(51) Sihar, N.; Tiong, T. Y.; Dee, C. F.; Ooi, P. C.; Hamzah, A. A.; Mohamed, M. A.; Majlis, B. Y. Ultraviolet Light-Assisted Copper Oxide Nanowires Hydrogen Gas Sensor. *Nanoscale Res. Lett.* **2018**, *13*, 4−9.

(52) Yamazoe, N.; Fuchigami, J.; Kishikawa, M.; Seiyama, T. Interactions of Tin Oxide Surface with O2, H2O AND H2. *Surf. Sci.* **1979**, *86*, 335−344.

(53) Lenaerts, S.; Roggen, J.; Maes, G. FT-IR Characterization of Tin Dioxide Gas Sensor Materials under Working Conditions. *Spectrochim. Acta Part A* **1995**, *51*, 883−894.

(54) Chang, S. C. Oxygen Chemisorption on Tin Oxide: Correlation Between Electrical Conductivity and Epr Measurements. *J. Vac. Sci. Technol.* **1979**, *17*, 366−369.

(55) Cooke, D. J.; Marmier, A.; Parker, S. C. Surface Structure of (1010) and (1120) Surfaces of ZnO with Density Functional Theory and Atomistic Simulation. *J. Phys. Chem. B* **2006**, *110*, 7985−7991.

(56) Wander, A.; Harrison, N. M. Ab-Initio Study of ZnO(1120). *Surf. Sci.* **2000**, *468*, 851−855.

(57) Grimme, S. Semiempirical GGA-Type Density Functional Constructed with a Long-Range Dispersion Correction. *Comput. Chem.* **2006**, *27*, 1787−1799.